Modeling and Verification of a Six-Phase Interior Permanent Magnet Synchronous Motor

Muluneh Lemma Woldesemayat, *Student Member, IEEE*, Heekwang Lee, *Student Member, IEEE*, Sangchul Won, *Member, IEEE*, and Kwanghee Nam, *Member, IEEE*

***Abstract*—In this paper, a new mathematical modeling for a six-phase interior permanent magnet synchronous motor (IPMSM) is presented. The proposed model utilizes two synchronous reference frames. First, the flux model in the $abcxyz$ frame is mapped into the stationary dq frames and then to two synchronous rotating frames. Then, differentiating the flux models, voltage equations are derived in rotating frames. Through this analysis, the interaction between the abc and xyz subsystems is properly described by a coupling matrix. The torque equation is also derived using the two reference current variables. Flux model was verified through FEM analysis. Experiments were done using a 100 kW six-phase IPMSM in a dynamo system. The validity of the torque equation was checked with some experimental results under a shorted condition on an xyz subsystem.**

***Index Terms*—Coordinate transformation, interior permanent magnet synchronous motor (IPMSM), rotor saliency, six-phase motor, two reference frames.**

I. Introduction

MULTIPHASE, higher than three, machines received a great attention in electric drive applications recently [1]. Based on the selection of motor types, permanent magnet synchronous motors (PMSMs) were generally preferred than induction motors from the point of view of efficiency, better power factor, and higher torque density [2], [3]. Multiphase PMSMs are preferred for their fault-tolerant nature, less torque pulsation, and little zero sequence harmonics [1], [4].

The modeling concept of multiphase motors was first introduced during the early development stage of inverter-fed ac drives [5]. Since then, various application research works were carried out in the areas such as ship propulsion, aircraft application, locomotive traction, and electric vehicles [5], [6]. Zhao and Lipo [7] demonstrated a modeling technique of six-phase induction machine in three two-dimensional (2-D) orthogonal subspaces and called it vector space decomposition (VSD). They claimed that the dynamics of the electromechanical energy conversion related machine variables were totally decoupled. Among the topologies of six-phase machines, asymmetrical thirty-degree phase shift winding configuration was preferred because of its minimal harmonic and torque pulsation [8]–[10].

The same VSD approach was applied to six-phase PMSM modeling [11]. Although the model included the coupling between the two sets of three-phase windings, it lacked analysis of saliency in the interior PMSM (IPMSM). Other modeling scheme [12], [13] treated the six-phase PMSM as two three-phase independent motors. Thus, the cross-coupling effects were ignored totally in the model. It was also reported that by increasing the number of poles and number of phases, efficiency and torque density could be improved [14].

In the control, six-phase PMSMs were regarded as two independent three-phase motors having two isolated neutral points [16]–[19]. The VSD was utilized often for vector control of six-phase PMSMs [16], [17]. Although VSD was a useful technique mostly adopted, it did not guarantee balanced current sharing between winding sets. Karttunen *et al*. [16] proposed a vector control scheme that offered improved dynamic performance and showed balanced current sharing. Additional improvement of the VSD scheme that adopted a proportional integral and resonant (second) controller for elimination of current unbalance in the $\alpha\beta$ subplane was presented in [17]. In the occurrence of open circuit, VSD became an incomplete decoupling mathematical model and a model predictive control technique was applied [19].

Usage of a split-phase motor such as dual three-phase motors lowered the back electromotive force (EMF), and as a result required less d-axis current for a flux weakening scheme in high-speed operation [20]. Use of additional degree of freedom of multiphase machines was presented in the area of grid-connected wind energy conversion systems and stand-alone applications [21]. Duran and Barrero [22] also presented the merits of multiphase machines in the faulty mode of operation. Moreover, open winding multiphase surface mounted permanent magnet synchronous motor (SPMSM) topology emphasizing on wide speed range and fault-tolerant operation in an electric vehicle propulsion system were presented in [23] and [24], respectively. However, such applications were realized at a cost of increased component counts and more expensive control.

For healthy operating condition of six-phase machines, VSD was preferred due to the effectiveness of modeling and control [16], [17]. However, in case of fault occurrence, VSD did not guarantee fault-tolerant and minimum torque pulsation re-

Manuscript received December 12, 2016; revised March 20, 2017 and August 20, 2017; accepted December 4, 2017. Date of publication December 13, 2017; date of current version July 15, 2018. Recommended for publication by Associate Editor E. Lomonova. *(Corresponding author: Kwanghee Nam.)*

The authors are with the Department of Electrical Engineering, Pohang University of Science and Technology, Pohang 790784, South Korea (e-mail: mulunehlemma@postech.ac.kr; draco@postech.ac.kr; won@postech.ac.kr; kwnam@postech.ac.kr).

Color versions of one or more of the figures in this paper are available online at http://ieeexplore.ieee.org.

Digital Object Identifier 10.1109/TPEL.2017.2782804

quirement [16], [17]. Additionally, analysis of motor saliency was not included in the mathematical model of six-phase machine adopted in [11]–[13], [16], and [17].

The purpose of this paper is to deduce a detailed and accurate mathematical model of the six-phase IPMSM. More emphasis is given on the proper analysis and inclusion of motor saliency in the IPMSM that was ignored in the existing VSD-based modeling. Furthermore, two-reference frame based model is pursued so that a simplified and accurate dynamic model is obtained. This paper is structured as follows. Sections II and III present mathematical modeling of six-phase PMSMs, FEM-based inductance calculation procedure, and flux and torque model verification. Section IV presents the IPMSM dynamic equation in a synchronous reference frame. Simulation by using FEM analysis and experimental results are shown in Section V. Finally, the general conclusion is presented in Section VI.

II. Mathematical Modeling of the IPMSM

Note that IPMSMs are characterized by the rotor saliency. It is illustrated by the flux path change caused by PM cavities when the rotor rotates. Therefore, the inductance appears as a function of rotor angle θ.

A. Review of a Three-Phase Machine

Before describing the whole flux linkage, we will review briefly how the rotor saliency is modeled in a three-phase IPMSM. First, it should be reminded that the relative permeability of PM is close to 1, so that the cavities for PM are seen as additional air gaps to the stator d-axis winding. Therefore, the d-axis inductance is smaller than the q-axis inductance. For mathematical treatment, the effective air gap of the IPMSM to a fixed direction, e.g., horizontal direction, is modeled simply by a function of the rotational angle θ such that $g(\theta) = \frac{1}{\gamma_0 - \gamma_1 \cos(2\theta)}$, where γ_0 and γ_1 are positive constants [25], [26]. For example, the inductance of a-phase winding will change as the rotor rotates. When the number of turns per phase is equal to N and the effective gap area A, the inductance appears as

$$L = \frac{\mu_0 A N^2}{2g(\theta)} = \frac{\mu_0 A N^2}{2}\left(\gamma_0 - \gamma_1 \cos(2\theta)\right) = L_{ms} - L_\delta \cos(2\theta) \tag{1}$$

where $L_{ms} \equiv \frac{\mu_0 A N^2}{2}\gamma_0$, $L_\delta \equiv \frac{\mu_0 A N^2}{2}\gamma_1$, and μ_0 is the permeability of free space. Note that L_{ms} is a static component, which corresponds to the average gap length, and L_δ determines the saliency. Note again that magnetization of PM is irrelevant in characterizing the saliency, since the PM relative permeability close to one and the superposition law are applied.

On the other hand, the PM flux linking to abc coils is described by $\boldsymbol{\psi}(\theta) = \psi_{\text{pm}}[\cos\theta, \cos(\theta - \frac{2\pi}{3}), \cos(\theta + \frac{2\pi}{3})]^T$ since the coils are shifted 120° from each other. Let the flux linkage and current of the abc coil be denoted by $\boldsymbol{\lambda}_{abc} = [\lambda_a, \lambda_b, \lambda_c]^T$ and $\mathbf{i}_{abc} = [i_a, i_b, i_c]^T$, respectively. Then, the flux linkage of the abc coil is described by

$$\boldsymbol{\lambda}_{abc} = \left[\mathbf{L} - L_\delta \mathbf{A}(\theta)\right]\mathbf{i}_{abc} + \boldsymbol{\psi}(\theta) \tag{2}$$

where

$$\mathbf{L} = \begin{bmatrix} L_m + L_{ls} & -\frac{L_m}{2} & -\frac{L_m}{2} \\ -\frac{L_m}{2} & L_m + L_{ls} & -\frac{L_m}{2} \\ -\frac{L_m}{2} & -\frac{L_m}{2} & L_m + L_{ls} \end{bmatrix},$$

$$\mathbf{A}(\theta) = \begin{bmatrix} \cos 2\theta & \cos\left(2\theta - \frac{2\pi}{3}\right) & \cos\left(2\theta + \frac{2\pi}{3}\right) \\ \cos\left(2\theta - \frac{2\pi}{3}\right) & \cos\left(2\theta + \frac{2\pi}{3}\right) & \cos 2\theta \\ \cos\left(2\theta + \frac{2\pi}{3}\right) & \cos(2\theta) & \cos\left(2\theta - \frac{2\pi}{3}\right) \end{bmatrix}.$$

$L_m + L_{ls}$ is the self-inductance, and L_{ls} is the leakage inductance.

Define by

$$\mathbf{T} = \frac{2}{3}\begin{bmatrix} 1 & -\frac{1}{2} & -\frac{1}{2} \\ 0 & \frac{\sqrt{3}}{2} & -\frac{\sqrt{3}}{2} \\ \frac{1}{2} & \frac{1}{2} & \frac{1}{2} \end{bmatrix} \tag{3}$$

a transformation matrix from the abc frame into a stationary $\alpha\beta 0$ frame. Let $\mathbf{i}_{\alpha\beta 0} = [i_\alpha, i_\beta, 0]^T = \mathbf{T}\mathbf{i}_{abc}$ and $\boldsymbol{\lambda}_{\alpha\beta 0} = [\lambda_\alpha, \lambda_\beta, 0]^T = \mathbf{T}[\lambda_a, \lambda_b, \lambda_c]^T$. Then, it follows from (2) that

$$\boldsymbol{\lambda}_{\alpha\beta 0} = \left[\mathbf{T}\mathbf{L}\mathbf{T}^{-1} - L_\delta \mathbf{T}\mathbf{A}(\theta)\mathbf{T}^{-1}\right]\mathbf{i}_{\alpha\beta 0} + \mathbf{T}\boldsymbol{\psi}(\theta). \tag{4}$$

Let 2-D variables be defined by $\boldsymbol{\lambda}_{\alpha\beta} = [\lambda_\alpha, \lambda_\beta]^T$ and $\mathbf{i}_{\alpha\beta} = [i_\alpha, i_\beta]^T$ using the first two components. Rewriting (4), we obtain

$$\boldsymbol{\lambda}_{\alpha\beta} = \mathbf{L}_g(\theta)\mathbf{i}_{\alpha\beta} + \boldsymbol{\psi}'_2(\theta) \tag{5}$$

where

$$\mathbf{L}_g(\theta) = \begin{bmatrix} L_M - \frac{3}{2}L_\delta \cos 2\theta & -\frac{3}{2}L_\delta \sin 2\theta \\ -\frac{3}{2}L_\delta \sin 2\theta & L_M + \frac{3}{2}L_\delta \cos 2\theta \end{bmatrix} = L_M \mathbf{I} - \frac{3}{2}L_\delta \mathbf{G}(\theta), \tag{6}$$

$$\mathbf{G}(\theta) = \begin{bmatrix} \cos 2\theta & \sin 2\theta \\ \sin 2\theta & -\cos 2\theta \end{bmatrix}, \tag{7}$$

$$\boldsymbol{\psi}'_2(\theta) = \psi_{\text{pm}}\begin{bmatrix} \cos\theta \\ \sin\theta \end{bmatrix} \tag{8}$$

and $\mathbf{I}$ is a 2×2 identity matrix and $L_M = \frac{3}{2}L_m + L_{ls}$. Note that $\mathbf{G}(\theta)$ is the matrix describing the reluctance depending on the rotor angle. Furthermore, $\boldsymbol{\lambda}_{\alpha\beta}$ transforms the synchronous dq frame via

$$\mathbf{F}(\theta) = \begin{bmatrix} \cos\theta & \sin\theta \\ -\sin\theta & \cos\theta \end{bmatrix} \tag{9}$$

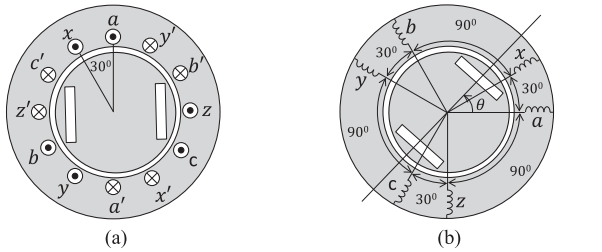

Fig. 1. Six-phase IPMSM: (a) coil layout and (b) direction of current vectors: Rotor angle θ refers to the angle between the direct axis of the rotor and the magnetic axis of phase a.

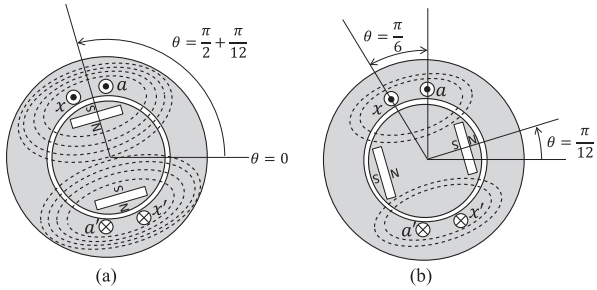

Fig. 2. Flux linking between a–a' and x–x' coils: (a) maximum when $\theta = \frac{\pi}{2} + \frac{\pi}{12}$, and (b) minimum when $\theta = \frac{\pi}{12}$.

such that

$$\boldsymbol{\lambda}_{dq}^{e} = \begin{bmatrix} L_M - \frac{3}{2}L_\delta & 0 \\ 0 & L_M + \frac{3}{2}L_\delta \end{bmatrix} \mathbf{i}_{dq}^{e} + \psi_{\text{pm}} \begin{bmatrix} 1 \\ 0 \end{bmatrix} \tag{10}$$

where $\boldsymbol{\lambda}_{dq}^{eT} = \mathbf{F}(\theta)[\lambda_\alpha,\, \lambda_\beta]^T$ and $\mathbf{i}_{dq}^{eT} = \mathbf{F}(\theta)[i_\alpha,\, i_\beta]^T$. These are well-established equations and appear in textbooks, for example, in [25] and [26].

B. Flux Linkage of the Six-Phase IPMSM

The six-phase motors considered in this paper have two sets of three-phase windings, which are separated by $\pi/6$ in electrical angle. The first group is named abc and the second group is xyz. Fig. 1 shows schematic diagram of a two-pole six-phase IPMSM.

The same modeling approach is applied here as in the three-phase case. In the following developments, we look at the windings of the six-phase IPMSM as two sets of three-phase windings. The reason is to take the advantage of similarities in the system matrices of the abc and xyz dynamics as much as possible. Otherwise, most equations will contain 6×6 matrices, thereby analysis turns out to be very difficult and lose the physical insights.

However, in the mathematical modeling, the six-phase machine is not a simple sum of two three-phase machines. There is a flux linking between the two sets of coils. Furthermore, a big difficulty lies on the fact that the rotor saliency is seen differently all the time for the two coil sets due to the phase difference.

The abc coil has two flux linking other than self-induction: one from the rotor PM and the other from the xyz coil. Let the current of the xyz coil be denoted by $\mathbf{i}_{xyz} = [i_x,\, i_y,\, i_z]^T$. Then, the flux linkage of the abc coil is described by

$$\boldsymbol{\lambda}_{abc} = \mathbf{L}\mathbf{i}_{abc} + \mathbf{M}\mathbf{i}_{xyz} - L_\delta \mathbf{A}(\theta)\mathbf{i}_{abc} - L_\delta \mathbf{A}\left(\theta - \frac{\pi}{12}\right)\mathbf{i}_{xyz} + \boldsymbol{\psi}(\theta) \tag{11}$$

where

$$\mathbf{M} = \frac{\sqrt{3}L_m}{2} \begin{bmatrix} 1 & -1 & 0 \\ 0 & 1 & -1 \\ -1 & 0 & 1 \end{bmatrix}. \tag{12}$$

Note that $\mathbf{M}$ is a static contribution to $\boldsymbol{\lambda}_{abc}$ made by the xyz coil shifted by $\pi/6$, and that the matrices $[\mathbf{L}_{abc} : \mathbf{M}]$ already appeared in six-phase SPMSMs [27], [28]. The PM contribution $\boldsymbol{\psi}(\theta)$ is also the same as that of the SPMSM. The reluctance part of the self-inductance $-L_\delta \mathbf{A}(\theta)$ is the same as in the case of the three-phase IPMSM.

However, we have the other reluctance component from the xyz coil, and it is described by $-L_\delta \mathbf{A}(\theta - \frac{\pi}{12})$. Fig. 2 illustrates two extremes: The flux linking from $x - x'$ to $a - a'$ is maximized when the PM center is aligned to the middle point of a and x coils, since the PM location gives a minimum hindrance to the flux, as shown in Fig. 2(a). The rotor angle is $\theta = \frac{\pi}{2} + \frac{\pi}{12}$, thereby $\mathbf{A}(\theta - \frac{\pi}{12})\big|_{\theta = \frac{\pi}{2} + \frac{\pi}{12}} = \mathbf{A}(\frac{\pi}{2})$. Note that $-L_\delta \mathbf{A}(\frac{\pi}{2})_{(1,1)} = -L_\delta \cos\pi = L_\delta$ yields the maximum value.

The other case is shown in Fig. 2(b) in which the PM location gives a maximum hindrance to the flux. Specifically, the flux linking from $x - x'$ to $a - a'$ is minimized when $\theta = \frac{\pi}{12}$. Then, $\mathbf{A}(\theta - \frac{\pi}{12})\big|_{\theta = \frac{\pi}{12}} = \mathbf{A}(0)$. Note that $-L_\delta \mathbf{A}(0)_{(1,1)} = -L_\delta \cos 0 = -L_\delta$ yields the minimum value. Therefore, the mutual inductance matrix between abc and xyz coils is modeled by $\mathbf{A}(\theta - \frac{\pi}{12})$ for arbitrary angle θ.

Let the flux linkage of the xyz coil denoted by $\boldsymbol{\lambda}_{xyz} = [\lambda_x,\, \lambda_y,\, \lambda_z]^T$. Following the similar reasoning, it follows that

$$\boldsymbol{\lambda}_{xyz} = \mathbf{L}\mathbf{i}_{xyz} + \mathbf{M}^T \mathbf{i}_{abc} - L_\delta \mathbf{A}\left(\theta - \frac{\pi}{12}\right)\mathbf{i}_{abc} - L_\delta \mathbf{A}\left(\theta - \frac{\pi}{6}\right)\mathbf{i}_{xyz} + \boldsymbol{\psi}\left(\theta - \frac{\pi}{6}\right). \tag{13}$$

It should be emphasized here that (13) is written with respect to the xyz frame. The rotor is $\pi/6$ behind in the xyz frame when the PM flux is aligned with the horizontal axis. Therefore, we have $\boldsymbol{\psi}(\theta - \frac{\pi}{6})$ for PM flux linkage. The reluctance part of the self-inductance of the xyz coil appears as $-L_\delta \mathbf{A}(\theta - \frac{\pi}{6})$ due to the rotor shifting from the reference position. On the other hand, the mutual flux from the abc coil is the same as the previous case (11).

Summing all together, we obtain a six-phase IPMSM flux model as

$$\begin{bmatrix} \boldsymbol{\lambda}_{abc} \\ \boldsymbol{\lambda}_{xyz} \end{bmatrix} = \begin{bmatrix} \mathbf{L} & \mathbf{M} \\ \mathbf{M}^T & \mathbf{L} \end{bmatrix} \begin{bmatrix} \mathbf{i}_{abc} \\ \mathbf{i}_{xyz} \end{bmatrix} - L_\delta \times \begin{bmatrix} \mathbf{A}(\theta) & \mathbf{A}\left(\theta - \frac{\pi}{12}\right) \\ \mathbf{A}\left(\theta - \frac{\pi}{12}\right) & \mathbf{A}\left(\theta - \frac{\pi}{6}\right) \end{bmatrix} \begin{bmatrix} \mathbf{i}_{abc} \\ \mathbf{i}_{xyz} \end{bmatrix} + \begin{bmatrix} \boldsymbol{\psi}(\theta) \\ \boldsymbol{\psi}\left(\theta - \frac{\pi}{6}\right) \end{bmatrix}. \tag{14}$$

III. Coordinate Transformations

Flux linkage of six-phase of the IPMSM (14) is different from that of the SPMSM due to the reluctance part. Dual coordinates are also used for d–q stationary and d–q synchronous frames, in the same way, we have used abc and xyz frames previously. Otherwise, we ought to use two different coordinate transformations in order to map abc and xyz variables into a single d–q coordinate frame. It makes the whole equations very complex, breaks up symmetries and similarities among many terms, and causes us to loose physical insights.

A. Flux Model in the Stationary Frame

Since we have two coil sets, the corresponding flux vectors are named differently in the stationary frame: We denote the variables with subscripts, (α, β) for the abc frame, whereas (γ, σ) for the xyz frame. Here, the same transformation matrix $\mathbf{T}$ is utilized for both abc and xyz variables, and let $\boldsymbol{\lambda}_{\gamma\sigma 0} \equiv [\lambda_\gamma, \lambda_\sigma, 0]^T \equiv \mathbf{T}\boldsymbol{\lambda}_{xyz}$ and $\mathbf{i}_{\gamma\sigma 0} \equiv [i_\gamma, i_\sigma, 0]^T = \mathbf{T}\mathbf{i}_{xyz}$. Then, two flux equations are obtained in the stationary frame from (14) such that

$$\boldsymbol{\lambda}_{\alpha\beta 0} = \mathbf{T}\mathbf{L}\mathbf{T}^{-1}\mathbf{i}_{\alpha\beta 0} + \mathbf{T}\mathbf{M}\mathbf{T}^{-1}\mathbf{i}_{\gamma\sigma 0} - L_\delta \mathbf{T}\mathbf{A}(\theta)\mathbf{T}^{-1}\mathbf{i}_{\alpha\beta 0} - L_\delta \mathbf{T}\mathbf{A}\left(\theta - \frac{\pi}{12}\right)\mathbf{T}^{-1}\mathbf{i}_{\gamma\sigma 0} + \mathbf{T}\boldsymbol{\psi}(\theta), \tag{15}$$

$$\boldsymbol{\lambda}_{\gamma\sigma 0} = \mathbf{T}\mathbf{L}\mathbf{T}^{-1}\mathbf{i}_{\gamma\sigma 0} + \mathbf{T}\mathbf{M}^T\mathbf{T}^{-1}\mathbf{i}_{\alpha\beta 0} - L_\delta \mathbf{T}\mathbf{A}\left(\theta - \frac{\pi}{6}\right)\mathbf{T}^{-1} \times \mathbf{i}_{\gamma\sigma 0} - L_\delta \mathbf{T}\mathbf{A}\left(\theta - \frac{\pi}{12}\right)\mathbf{T}^{-1}\mathbf{i}_{\alpha\beta 0} + \mathbf{T}\boldsymbol{\psi}\left(\theta - \frac{\pi}{6}\right). \tag{16}$$

Here, it is assumed that $\mathbf{i}_{abc}$ and $\mathbf{i}_{xyz}$ are balanced, so that zero was put into the third component. Disregarding the zero component, we let $\boldsymbol{\lambda}_{\gamma\sigma} \equiv [\lambda_\gamma, \lambda_\sigma]^T$ and $\mathbf{i}_{\gamma\sigma} \equiv [i_\gamma, i_\sigma]^T$. Then, (15) and (16) can be rewritten as

$$\boldsymbol{\lambda}_{\alpha\beta} = \mathbf{L}_g(\theta)\mathbf{i}_{\alpha\beta} + \mathbf{M}_g(\theta)\mathbf{i}_{\gamma\sigma} + \boldsymbol{\psi}_2'(\theta), \tag{17}$$

$$\boldsymbol{\lambda}_{\gamma\sigma} = \mathbf{L}_g\left(\theta - \frac{\pi}{6}\right)\mathbf{i}_{\gamma\sigma} + \mathbf{M}_g^T(\theta)\mathbf{i}_{\alpha\beta} + \boldsymbol{\psi}_2'\left(\theta - \frac{\pi}{6}\right) \tag{18}$$

where

$$\mathbf{M}_g(\theta) = \begin{bmatrix} \frac{3\sqrt{3}L_m}{4} - \frac{3}{2}L_\delta \cos\left(2\theta - \frac{\pi}{6}\right) & -\frac{3L_m}{4} - \frac{3}{2}L_\delta \sin\left(2\theta - \frac{\pi}{6}\right) \\ \frac{3L_m}{4} - \frac{3}{2}L_\delta \sin\left(2\theta - \frac{\pi}{6}\right) & \frac{3\sqrt{3}L_m}{4} + \frac{3}{2}L_\delta \cos\left(2\theta - \frac{\pi}{6}\right) \end{bmatrix} = \left[\mathbf{M}_s - \frac{3}{2}L_\delta \mathbf{G}\left(\theta - \frac{\pi}{12}\right)\right], \tag{19}$$

$$\mathbf{M}_s = \frac{3}{4}L_m \begin{bmatrix} \sqrt{3} & -1 \\ 1 & \sqrt{3} \end{bmatrix}. \tag{20}$$

Note that the flux linkages are expressed neatly with two types of functions: $\mathbf{L}_g(\theta)$ states the self-inductance, whereas $\mathbf{M}_g(\theta)$ the mutual inductance between the coil groups. Note also that $\mathbf{L}_g(\theta)$, $\mathbf{G}(\theta)$, and $\boldsymbol{\psi}_2'(\theta)$ were already defined in (6), (7), and (8), respectively. Equations (17) and (18) show a great symmetry between the two coil sets shifted by $\frac{\pi}{6}$.

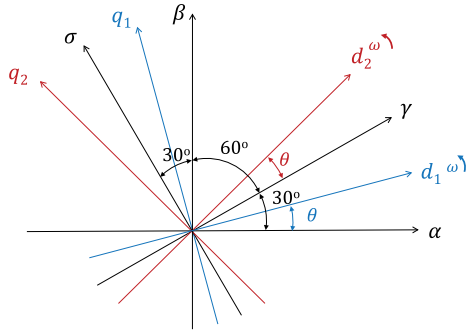

Fig. 3. Six-phase IPMSM in two stationary and two synchronous frames.

B. Flux Model in Synchronous Reference Frames

The two flux vectors $\boldsymbol{\lambda}_{\alpha\beta}$ and $\boldsymbol{\lambda}_{\gamma\sigma}$ have $\pi/6$ phase difference. We apply the same map $\mathbf{F}(\theta)$ in order to map them into the synchronous reference frame. Voltage, current, and flux variables are mapped from the stationary rectangular frames via $\mathbf{F}(\theta)$. To distinguish two vectors, we let $\boldsymbol{\lambda}_{dq1}^e = [\lambda_{d1}^e, \lambda_{q1}^e]^T = \mathbf{F}(\theta)\boldsymbol{\lambda}_{\alpha\beta}$, $\boldsymbol{\lambda}_{dq2}^e = [\lambda_{d2}^e, \lambda_{q2}^e]^T = \mathbf{F}(\theta)\boldsymbol{\lambda}_{\gamma\sigma}$, $\mathbf{i}_{dq1}^e = [i_{d1}^e, i_{q1}^e]^T = \mathbf{F}(\theta)\mathbf{i}_{\alpha\beta}$, and $\mathbf{i}_{dq2}^e = [i_{d2}^e, i_{q2}^e]^T = \mathbf{F}(\theta)\mathbf{i}_{\gamma\sigma}$. Fig. 3 shows the two reference axes for stationary and synchronous coordinate frames. (d_1, q_1) are the reference axes for the abc coil, whereas (d_2, q_2) are the other reference axes for the xyz coil. It follows from (17) and (18) that

$$\boldsymbol{\lambda}_{dq1}^e = \boldsymbol{L}_{dq1}\mathbf{i}_{dq1}^e + \mathbf{M}_f\mathbf{i}_{dq2}^e + \boldsymbol{\psi}_{dq1}^e, \tag{21}$$

$$\boldsymbol{\lambda}_{dq2}^e = \boldsymbol{L}_{dq2}\mathbf{i}_{dq2}^e + \mathbf{M}_f^T\mathbf{i}_{dq1}^e + \boldsymbol{\psi}_{dq2}^e \tag{22}$$

where $\boldsymbol{\psi}_{dq1}^e \equiv \mathbf{F}(\theta)\boldsymbol{\psi}'(\theta) = \psi_{\text{pm}}[1, 0]^T$, $\boldsymbol{\psi}_{dq2}^e \equiv \mathbf{F}(\theta)\boldsymbol{\psi}'(\theta - \frac{\pi}{6}) = \psi_{\text{pm}}[\frac{\sqrt{3}}{2}, -\frac{1}{2}]^T$,

$$\mathbf{F}(\theta)\mathbf{L}_g(\theta)\mathbf{F}^{-1}(\theta) = \begin{bmatrix} L_M - \frac{3}{2}L_\delta & 0 \\ 0 & L_M + \frac{3}{2}L_\delta \end{bmatrix} \equiv \boldsymbol{L}_{dq1}, \tag{23}$$

$$\mathbf{F}(\theta)\mathbf{L}_g\left(\theta - \frac{\pi}{6}\right)\mathbf{F}^{-1}(\theta) = \begin{bmatrix} L_M - \frac{3}{4}L_\delta & \frac{3\sqrt{3}}{4}L_\delta \\ \frac{3\sqrt{3}}{4}L_\delta & L_M + \frac{3}{4}L_\delta \end{bmatrix} \equiv \boldsymbol{L}_{dq2}, \tag{24}$$

$$\mathbf{F}(\theta)\mathbf{M}_g(\theta)\mathbf{F}^{-1}(\theta) = \frac{3}{4}\begin{bmatrix} \sqrt{3}(L_m - L_\delta) & -(L_m - L_\delta) \\ (L_m + L_\delta) & \sqrt{3}(L_m + L_\delta) \end{bmatrix} \equiv \mathbf{M}_f, \tag{25}$$

$$\mathbf{F}(\theta)\mathbf{M}_g^T(\theta)\mathbf{F}^{-1}(\theta) = \mathbf{M}_f^T. \tag{26}$$

It must be reminded that $L_M = \frac{3}{2}L_m + L_{ls}$. It is also remarkable from (19) and (25) that the similarity transformation of $\mathbf{M}_g^T(\theta)$ by $\mathbf{F}(\theta)$ yields the constant matrix $\mathbf{M}_f$. Specifically,

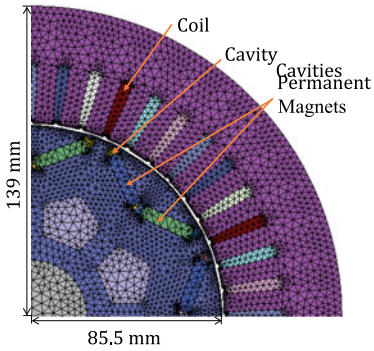

Fig. 4. 2-D mesh model of an eight-pole six-phase IPMSM.

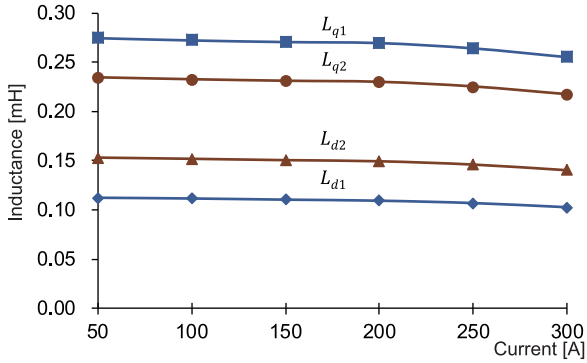

Fig. 5. FEM-based inductance calculations.

TABLE I
FLUX LINKAGES FOR A SPECIFIC POSITION $\theta = \frac{\pi}{6}$

Excitation current $\mathbf{i}_{abcxyz}$ (A)	λ'_a (mWb)	λ'_b (mWb)	λ'_c (mWb)
$[50, 0, 0, 0, 0, 0]^T$	6.76	−2.92	1.14
$[100, 0, 0, 0, 0, 0]^T$	13.35	−5.80	2.24
$[150, 0, 0, 0, 0, 0]^T$	19.86	−8.68	3.35
$[200, 0, 0, 0, 0, 0]^T$	26.31	−11.60	4.45
$[250, 0, 0, 0, 0, 0]^T$	32.06	−14.27	5.42
$[300, 0, 0, 0, 0, 0]^T$	36.89	−16.73	6.21

the θ-dependence disappeared completely. Note further that L_{d1}, L_{q1} and L_{d2}, L_{q2} are the inductances in the synchronous reference frame. They are different, though a single rotor is shared. The reason is that the rotor axis is seen differently by the two coil sets. It is worthwhile to note that $L_{q1} - L_{d1} = 3L_\delta$, whereas $L_{q2} - L_{d2} = \frac{3}{2}L_\delta$. In other words, $L_{d1} < L_{d2}$ and $L_{q1} > L_{q2}$. Therefore, $L_{q1}/L_{d1} > L_{q2}/L_{d2}$, i.e., the saliency is larger with respect to the abc coil than to the xyz coil.

C. Inductance Determination Through FEM Analysis

It is possible to compute the flux linkage of a coil via FEM analysis. Fig. 4 shows a 2-D mesh model of an eight-pole six-phase IPMSM in which magnets are arranged in a V-shape in each pole. The outer diameter of the stator and rotor is 278 and 171 mm, respectively. The stack length is 120 mm and air gap height is 0.8 mm.

For the purpose of obtaining the inductances, special cases are considered when only i_a flows. FEM calculations were done for different i_a s and a specific standstill rotor position $\theta = \frac{\pi}{6}$. Table I shows the computed results. Since the current to flux relation is given by

$$\begin{bmatrix}\lambda'_a\\ \lambda'_b\\ \lambda'_c\end{bmatrix} = \begin{bmatrix}\lambda_a\\ \lambda_b\\ \lambda_c\end{bmatrix} - \psi_{\text{pm}}\begin{bmatrix}\cos\theta\\ \cos\left(\theta - \frac{2\pi}{3}\right)\\ \cos\left(\theta + \frac{2\pi}{3}\right)\end{bmatrix} = \begin{bmatrix}L_m + L_{ls}\\ -0.5L_m\\ -0.5L_m\end{bmatrix} i_a - L_\delta \begin{bmatrix}0.5\\ 0.5\\ -1\end{bmatrix} i_a \tag{27}$$

we can find L_m, L_{ls}, and L_δ easily from the above-mentioned three equations. Further utilizing (23) and (24), L_{d1}, L_{q1}, L_{d2}, and L_{q2} were also obtained, and the results are depicted in Fig. 5. Note that L_q 's are saturated more at high currents.

To prove the validity of the flux model, analytic computations are compared with the FEM data for different currents and different rotor angles. Table II shows analytic results based on (14), as well as the FEM results. Note that they show good agreements at arbitrary angles although the analytic model was developed with a simplified air gap function (1).

IV. IPMSM DYNAMIC EQUATION IN A SYNCHRONOUS REFERENCE FRAME

It is necessary to develop a dynamic equation in the synchronous frame for flux-oriented current control. The reference frame is rotating in synchronism with $\theta = \omega t$. It is assumed here that the rotor flux is aligned with the $d1$-axis. Then, the $d2$-axis is $\frac{\pi}{6}$-ahead of the $d1$-axis.

A. Voltage Equation

The voltage equations are derived directly by differentiating (21) and (22):

$$\mathbf{v}^e_{dq1} \equiv r_s\mathbf{i}^e_{dq1} + \mathbf{F}(\theta)\frac{d}{dt}(\mathbf{F}^{-1}(\theta)\boldsymbol{\lambda}^e_{dq1}) = r_s\mathbf{i}^e_{dq1} + \omega\mathbf{F}(\theta)\frac{\partial\mathbf{F}^{-1}(\theta)}{\partial\theta}\boldsymbol{\lambda}^e_{dq1} + \frac{d}{dt}\boldsymbol{\lambda}^e_{dq1}, \tag{28}$$

$$\mathbf{v}^e_{dq2} \equiv r_s\mathbf{i}^e_{dq2} + \mathbf{F}(\theta)\frac{d}{dt}(\mathbf{F}^{-1}(\theta)\boldsymbol{\lambda}^e_{dq2}) = r_s\mathbf{i}^e_{dq2} + \omega\mathbf{F}(\theta)\frac{\partial\mathbf{F}^{-1}(\theta)}{\partial\theta}\boldsymbol{\lambda}^e_{dq2} + \frac{d}{dt}\boldsymbol{\lambda}^e_{dq2} \tag{29}$$

where $\mathbf{v}^e_{dq1} = [v^e_{d1}, v^e_{q1}]^T$, $\mathbf{v}^e_{dq2} = [v^e_{d2}, v^e_{q2}]^T$, and r_s is the coil resistance per phase. Note that

$$\mathbf{F}(\theta)\frac{\partial\mathbf{F}^{-1}(\theta)}{\partial\theta} = \begin{bmatrix}0 & -1\\ 1 & 0\end{bmatrix} \equiv \mathbf{J}, \quad \boldsymbol{\psi}'^e_{dq1} \equiv \mathbf{J}\boldsymbol{\psi}^e_{dq1} = \psi_{\text{pm}}\begin{bmatrix}0\\ 1\end{bmatrix}, \quad \text{and} \quad \boldsymbol{\psi}'^e_{dq2} \equiv \mathbf{J}\boldsymbol{\psi}^e_{dq2} = \psi_{\text{pm}}\begin{bmatrix}\frac{1}{2}\\ \frac{\sqrt{3}}{2}\end{bmatrix}.$$

TABLE II
VERIFICATION OF FLUX MODEL FOR DIFFERENT CURRENTS AND ANGLES

Current $\mathbf{i}_{abcxyz}$ (A)	θ	Method	λ_a (mWb)	λ_b (mWb)	λ_c (mWb)	λ_x (mWb)	λ_y (mWb)	λ_z (mWb)
$[5, 5, -10, 5, 5, -10]^T$	$\frac{160\pi}{180}$	FEM	1.49	3.17	−4.31	3.04	1.49	−4.32
		Analytical	1.40	2.90	−4.20	2.90	1.30	−4.20
$[0, 5, 0, 0, 5, 0]^T$	$\frac{77\pi}{180}$	FEM	−0.80	1.59	−0.24	−0.27	1.59	−0.89
		Analytical	−0.82	1.50	−0.22	−0.35	1.50	−0.73

The back EMFs $\boldsymbol{\psi}'^{e}_{dq1}$ and $\omega\boldsymbol{\psi}'^{e}_{dq2}$ are different since the rotor PM flux angle is seen differently in the two coordinates. On the other hand, it follows from (21) and (22) that

$$\frac{d}{dt}\boldsymbol{\lambda}^e_{dq_1} = \boldsymbol{L}_{dq1}\frac{d}{dt}\mathbf{i}^e_{dq1} + \mathbf{M}_f\frac{d}{dt}\mathbf{i}^e_{dq2}, \tag{30}$$

$$\frac{d}{dt}\boldsymbol{\lambda}^e_{dq_2} = \boldsymbol{L}_{dq2}\frac{d}{dt}\mathbf{i}^e_{dq2} + \mathbf{M}^T_f\frac{d}{dt}\mathbf{i}^e_{dq1}. \tag{31}$$

Thus, (28) and (29) are rewritten as

$$\mathbf{v}^e_{dq1} = r_s\mathbf{i}^e_{dq1} + \boldsymbol{L}_{dq1}\frac{d}{dt}\mathbf{i}^e_{dq1} + \omega\mathbf{J}\boldsymbol{L}_{dq1}\mathbf{i}^e_{dq1} + \omega\boldsymbol{\psi}'^{e}_{dq1} + \mathbf{M}_f\frac{d}{dt}\mathbf{i}^e_{dq2} + \omega\mathbf{J}\mathbf{M}_f\mathbf{i}^e_{dq2}, \tag{32}$$

$$\mathbf{v}^e_{dq2} = r_s\mathbf{i}^e_{dq2} + \boldsymbol{L}_{dq2}\frac{d}{dt}\mathbf{i}^e_{dq2} + \omega\mathbf{J}\boldsymbol{L}_{dq2}\mathbf{i}^e_{dq2} + \omega\boldsymbol{\psi}'^{e}_{dq2} + \mathbf{M}^T_f\frac{d}{dt}\mathbf{i}^e_{dq1} + \omega\mathbf{J}\mathbf{M}^T_f\mathbf{i}^e_{dq1} \tag{33}$$

where

$$\mathbf{J}\mathbf{M}_f = \frac{3}{4}\begin{bmatrix} -(L_m+L_\delta) & -\sqrt{3}(L_m+L_\delta) \\ \sqrt{3}(L_m-L_\delta) & -(L_m-L_\delta) \end{bmatrix},$$

$$\mathbf{J}\mathbf{M}^T_f = \frac{3}{4}\begin{bmatrix} (L_m-L_\delta) & -\sqrt{3}(L_m+L_\delta) \\ \sqrt{3}(L_m-L_\delta) & (L_m+L_\delta) \end{bmatrix}.$$

Note that (32) and (33) are the voltage equations on different synchronous frames $(d1^e, q1^e)$ and $(d2^e, q2^e)$. The voltages $\omega\mathbf{J}\boldsymbol{L}_{dq1}\mathbf{i}^e_{dq1}$ and $\omega\mathbf{J}\boldsymbol{L}_{dq2}\mathbf{i}^e_{dq2}$ are the conventional couplings between d and q axes in their own frames. However, $\omega\mathbf{J}\mathbf{M}^T_f\mathbf{i}^e_{dq1}$ and $\omega\mathbf{J}\mathbf{M}_f\mathbf{i}^e_{dq2}$ are the coupling voltages between the two coil sets. Furthermore, there are other couplings $\mathbf{M}_f\frac{d}{dt}\mathbf{i}^e_{dq2}$ and $\mathbf{M}^T_f\frac{d}{dt}\mathbf{i}^e_{dq1}$ that depend on the current derivatives. This dynamic model is different from the past model such as VSD [16], [17], since the mutual interaction between the coil sets is properly introduced with reluctance.

B. Torque Model

Electromagnetic torque equation T_e is obtained by the cross product of stator flux and stator current, i.e., in general, torque is equal to $\frac{3P}{4}\boldsymbol{\lambda}^e_{dq}\times\mathbf{i}^e_{dq}$ [26]. The cross product can be replaced by a complex number operation such that $\mathrm{Im}\{\mathbf{i}^e_{dq}\cdot\boldsymbol{\lambda}^{e*}_{dq}\}$, where $\mathrm{Im}\{\cdot\}$ denotes the imaginary part and $*$ implies the complex conjugate.

In the six-phase IPMSM, we have two current vectors in the air gap; $\mathbf{i}^e_{dq1}$ and $\mathbf{i}^e_{dq2}$. But the latter is $\frac{\pi}{6}$ advanced from the former. Therefore, the air gap current vector is $\mathbf{i}^e_{dq1} + e^{j\frac{\pi}{6}}\mathbf{i}^e_{dq2}$, as shown in Fig. 6(a). Similarly, it is necessary to consider the flux sum $\boldsymbol{\lambda}_g$ in the air gap [see Fig. 6(b)] as

$$\boldsymbol{\lambda}_g = (\mathbf{L}_{dq1}\mathbf{i}^e_{dq1} + \boldsymbol{\psi}^e_{dq1}) + e^{j\frac{\pi}{6}}(\mathbf{L}_{dq2}\mathbf{i}^e_{dq2}). \tag{34}$$

Therefore, the torque of the P-pole six-phase IPMSM is equal to

$$T_e = \frac{3P}{4}\mathrm{Im}\big\{\big(\mathbf{i}^e_{dq1} + e^{j\frac{\pi}{6}}\mathbf{i}^e_{dq2}\big)\cdot\big((\mathbf{L}_{dq1}\mathbf{i}^e_{dq1} + \boldsymbol{\psi}^e_{dq1}) + [e^{j\frac{\pi}{6}}(\mathbf{L}_{dq2}\mathbf{i}^e_{dq2})]\big)^*\big\} = T_{e1} + T_{e2} + T_{e12} \tag{35}$$

where

$$\begin{aligned} T_{e1} &= \frac{3P}{4}\mathrm{Im}\big\{\mathbf{i}^e_{dq1}\cdot(\mathbf{L}_{dq1}\mathbf{i}^e_{dq1} + \boldsymbol{\psi}^e_{dq1})^*\big\} \\ &= \frac{3P}{4}\left(\psi_{\mathrm{pm}}i^e_{q1} + (L_{d1}-L_{q1})i^e_{d1}i^e_{q1}\right), \end{aligned} \tag{36}$$

$$\begin{aligned} T_{e2} &= \frac{3P}{4}\mathrm{Im}\big\{e^{j\frac{\pi}{6}}\mathbf{i}^e_{dq2}\cdot(e^{j\frac{\pi}{6}}\mathbf{L}_{dq2}\mathbf{i}^e_{dq2} + \boldsymbol{\psi}^e_{dq1})^*\big\} \\ &= \frac{3P}{4}\left(\psi_{\mathrm{pm}}\left(\frac{\sqrt{3}}{2}i^e_{q2} + \frac{i^e_{d2}}{2}\right) + (L_{d2}-L_{q2})i^e_{d2}i^e_{q2} + \frac{3\sqrt{3}}{4}L_\delta(i^{e2}_{q2} - i^{e2}_{d2})\right), T_{e12} = \frac{3P}{4}\mathrm{Im}\big\{\mathbf{i}^e_{dq1} \\ &\quad\cdot e^{-j\frac{\pi}{6}}(\mathbf{L}_{dq2}\mathbf{i}^e_{dq2})^*\big\} + \frac{3P}{4}\mathrm{Im}\big\{e^{j\frac{\pi}{6}}\mathbf{i}^e_{dq2}\cdot(\mathbf{L}_{dq1}\mathbf{i}^e_{dq1})^*\big\} \\ &= \frac{3P}{4}\Bigg(\frac{1}{2}(L_{d1}-L_{d2}-\frac{9}{4}L_\delta)i^e_{d1}i^e_{d2} \\ &\quad + \frac{1}{2}\left(L_{q1}-L_{q2}+\frac{9}{4}L_\delta\right)i^e_{q1}i^e_{q2} \\ &\quad + \frac{\sqrt{3}}{2}\left(L_{d1}-L_{q2}-\frac{3}{4}L_\delta\right)i^e_{d1}i^e_{q2} \\ &\quad + \frac{\sqrt{3}}{2}\left(L_{d2}-L_{q1}-\frac{3}{4}L_\delta\right)i^e_{q1}i^e_{d2}\Bigg). \end{aligned} \tag{37}$$

Note that T_{e1} represents a torque component by the abc coil, and T_{e2} by the xyz coil. T_{e1} has the normal expression of the three-phase IPMSM. In case of T_{e2}, it is necessary to consider that the PM flux is not aligned with the $d2$-axis. When $i^e_{d2} = 0$, T_{e2} has a reduced magnetic torque component $\psi_{\mathrm{pm}}\frac{\sqrt{3}}{2}i^e_{q2}$ along with reluctance component $\frac{3\sqrt{3}}{4}L_\delta i^{e2}_{q2}$. Note also that T_{e12} is the

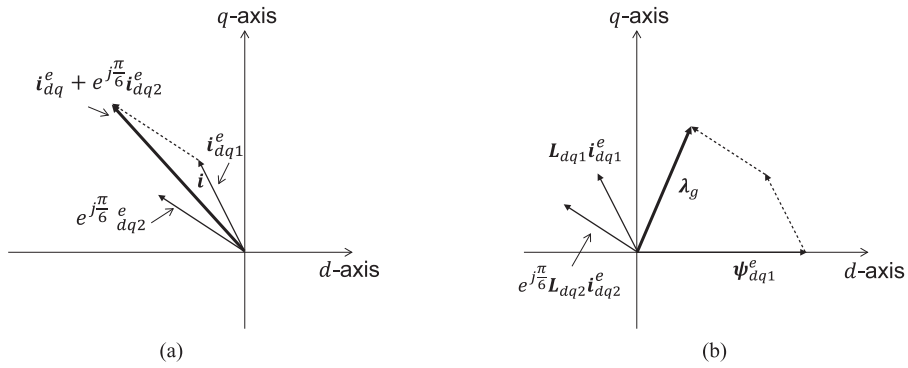

Fig. 6. Vector sum in the air gap of a six-phase IPMSM: (a) current sum and (b) flux sum.

TABLE III
FEM VERSUS ANALYTIC TORQUE COMPARISON

Cases	Excitation current (A)				Flux (Wb)	Torque (N·m)		% Error
	i^e_{d1}	i^e_{q1}	i^e_{d2}	i^e_{q2}	ψ_{pm}	FEM	Analytic	
Case I	0	33	0	0	0.051	10.09	10.1	0.08
Case II	0	0	0	66	0.051	19.3	19.33	0.1
Case III	0	132	0	132	0.051	83.83	91.04	8.6

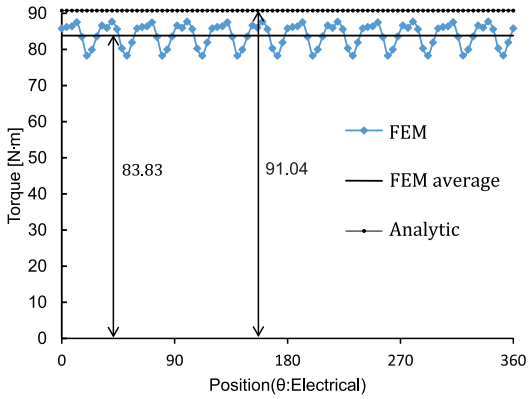

Fig. 7. FEM versus analytic torque for case III ($i^e_{q1} = 132$ A $i^e_{q2} = 132$ A).

remaining reluctance torque components caused by the saliency of the rotor.

Fig. 8 depicts the proposed six-phase IPMSM dynamics (32), (33), and torque model (35). Two subdynamics of abc and xyz are interlinked by the dotted line. During steady-state operation, the coupling terms induced by the current differentials $\mathbf{M}_f \frac{d}{dt}\mathbf{i}^e_{dq2}$ and $\mathbf{M}^T_f \frac{d}{dt}\mathbf{i}^e_{dq1}$ can be ignored. In the steady state, $\omega \mathbf{J}\mathbf{M}_f \mathbf{i}^e_{dq2}$ and $\omega \mathbf{J}\mathbf{M}^T_f \mathbf{i}^e_{dq1}$ link two subsystems, which is a characteristic feature of the six-phase IPMSM.

Table III shows torque calculation results obtained by FEM and the above-mentioned analytic equation under various current conditions. In calculating the analytic torque, inductance data shown in Fig. 5 were used. A small difference in case III seem to be caused by core saturation. Note that the two results are quite close, showing the validity of the equation. Fig. 7 shows torque plot versus electrical angle for case III.

TABLE IV
SIX-PHASE IPMSM PARAMETERS

Parameters	Value	Parameters	Value
Number of poles (P)	8	Rated speed	3000 r/min
Max. power	100 kW	Max. torque	320 N·m
Max. current (rms)	320 A	r_s at 100 °C	11.2 mΩ
PM flux linkage	0.05 Wb	DC-link voltage (V_{dc})	360 V

V. EXPERIMENTAL VERIFICATION OF THE PROPOSED MODEL

Experiments were performed using a six-phase IPMSM developed with the parameters shown in Table IV. Fig. 9 shows the dynamometer, which governs the shaft speed and loading conditions, six-phase IPMSM, and two inverters.

Fig. 10(a) and (b) shows FEM results of line-to-line back EMF at 3000 r/min. A phase difference of 30° can be checked from abc and xyz EMFs. Fig. 10(c) shows the corresponding experimental result that matches well with the simulation result.

Fig. 11(a) and (c) shows the current responses when the current command was set $(i^{*e}_{q1},\ i^{*e}_{q2}) = (32.5, 32.5)$ A at 1000 r/min. Currents i_a and i_x are equally shared with 30° phases difference. At this time, 20 N·m shaft torque was produced. According to the torque equation (39), torque was calculated as 19.52 N·m. Fig. 11(b) and (d) shows another case when producing the same torque at 1000 r/min with $(i^{*e}_{d1},\ i^{*e}_{q1}) = (-58, 58)$ A, $(i^{*e}_{d2},\ i^{*e}_{q2}) = (0, 0)$ A.

To verify the correctness of motor parameters, an experiment was performed under a shorted condition on xyz coils. The abc coils were connected to a three-phase inverter, but the xyz coils were shorted. The shaft was run at a fixed speed 100 r/min by the dynamometer motor. The inverter current commands were set to zero initially, but the q-axis current command i^{*e}_{q1} was changed to 100 A in a step manner after 500 ms. Fig. 12(a) and (b) shows i^e_{d1} and i^e_{q1}, respectively. Fig. 12(d)–(f) shows the corresponding $\mathbf{i}^e_{dq2}$ and x-phase current i_x. Finally, Fig. 12(c) shows the shaft torque. Since the shaft was rotating, the xyz coils were in a generation state. It is also to be noted that the speed was set at 100 r/min to avoid excessively large xyz currents. Note that (i^e_{d1}, i^e_{q1}) showed a well-regulated behavior, whereas (i^e_{d2}, i^e_{q2}) ripple currents since xyz coils were shorted without an inverter.

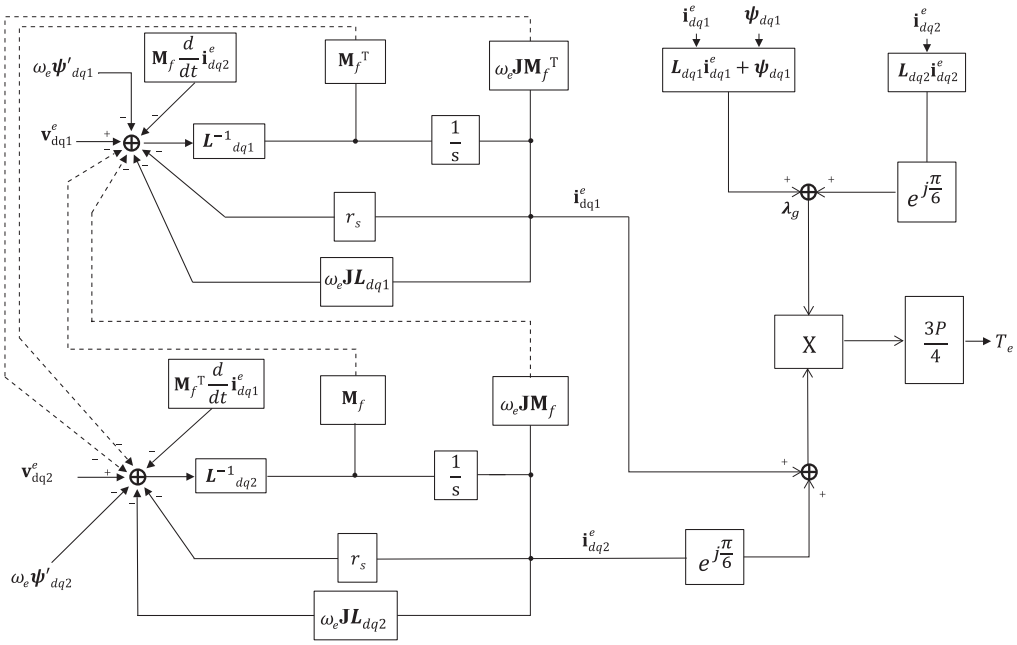

Fig. 8. Block diagram representing six-phase IPMSM dynamics.

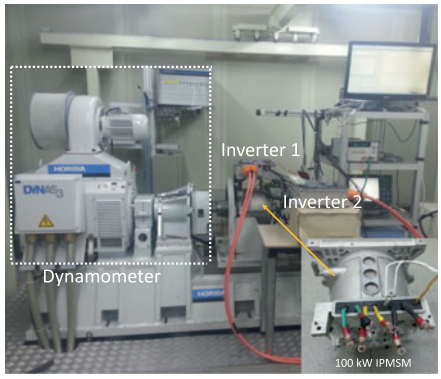

Fig. 9. Experimental environment: dynamometer, six-phase IPMSM, and two inverters.

A. Inductance Calculation

Inductances can be estimated experimentally from the above-mentioned shorted condition on xyz coils. Since xyz coils are shorted, $\mathbf{v}^e_{dq2}=0$. Further assuming the steady-state condition, we obtain from (33) that

$$\mathbf{i}^e_{dq2}=\left[\,r_s\mathbf{I}+\omega_e\mathbf{J}\boldsymbol{L}_{dq2}\quad\right]^{-1}\left[-\omega_e\mathbf{J}\mathbf{M}_f^T\mathbf{i}^e_{dq1}-\omega_e\psi'^e_{dq2}\quad\right]. \tag{38}$$

Substituting (24) into (38), L_M and L_δ can be obtained when $(i^e_{d1},i^e_{q1})=(0,0)$ A. Inserting $\omega_e=41.9$ rad/s, $r_s=11.2\,\mathrm{m}\Omega$, $(i^e_{d2},i^e_{q2})=(-185,-51)$ A, and $\psi_{\mathrm{pm}}=0.051$ Wb, we obtain

$$\begin{bmatrix}L_M\\L_\delta\end{bmatrix}=\begin{bmatrix}-\omega_e i^e_{q2} & -\frac{3}{4}\left(\omega_e i^e_{q2}+\sqrt{3}\omega_e i^e_{d2}\right)\\ \omega_e i^e_{d2} & -\frac{3}{4}\left(\omega_e i^e_{d2}-\sqrt{3}\omega_e i^e_{q2}\right)\end{bmatrix}^{-1}$$
$$\times\left(-r_s\mathbf{i}^e_{dq2}-\omega_e\psi'^e_{dq2}\right)=\begin{bmatrix}185\\52\end{bmatrix}\mu\mathrm{H}.$$

TABLE V
INDUCTANCES DATA COMPARISON

FEM analysis ($i_a=250$ A)			Experiments (xyz coil shorted)		
L_m	L_{ls}	L_δ	L_m	L_{ls}	L_δ
61.6 μH	92.7 μH	52 μH	59.5 μH	95.6 μH	52 μH

Therefore, $L_{d2}=146\,\mu$H and $L_{q2}=224\,\mu$H.

Now, we consider the second-phase experiment where $(i^e_{d1},i^e_{q1})=(0,100)$ A. Let

$$\Delta\mathbf{i}^e_{dq2}\equiv\mathbf{i}^e_{dq2}\Big|_{\mathbf{i}^e_{dq1}=(0,100)}-\mathbf{i}^e_{dq2}\Big|_{\mathbf{i}^e_{dq1}=(0,0)}=\begin{bmatrix}30\\-38\end{bmatrix}\mathrm{A}.$$

It follows from (38) that

$$\mathbf{M}_f^T\mathbf{i}^e_{dq1}=-\mathbf{J}^{-1}\left[\frac{r_s}{\omega_e}\mathbf{I}+\mathbf{J}\boldsymbol{L}_{dq2}\right]\Delta\mathbf{i}^e_{dq2}=\begin{bmatrix}0.0083\\0.0145\end{bmatrix}. \tag{39}$$

Since $(i^e_{d1},i^e_{q1})=(0,100)$ A, we obtain from (39) $L_m=59.5\,\mu$H. The inductance data obtained from experimental results are compared with those from FEM analysis in Table V. Note that when xyz phases are shorted, very high current flows in xyz phases [see Fig. 12(e)]. Therefore, $i_a=250$ A is used for FEM-based inductance calculation so that equivalent condition could be achieved for inductance comparison.

B. Verification Via Torque Comparison

Based on the inductance estimates shown in Table V, we obtain L_{d1}, L_{q1}, L_{d2}, and L_{q2}, as shown in Table VI.

With the inductances in Table VI, torque can be computed componentwise: T_{e1}, T_{e2}, and T_{e12}. For the analysis of torque when xyz phases are shorted, it is reasonable to exclude $\frac{3P}{4}\mathrm{Im}\{\mathbf{i}^e_{dq1}\cdot(e^{j\frac{\pi}{6}}\mathbf{M}_f^T\mathbf{i}^e_{dq1})^*\}$, $\frac{3P}{4}\mathrm{Im}\{e^{j\frac{\pi}{6}}\cdot$

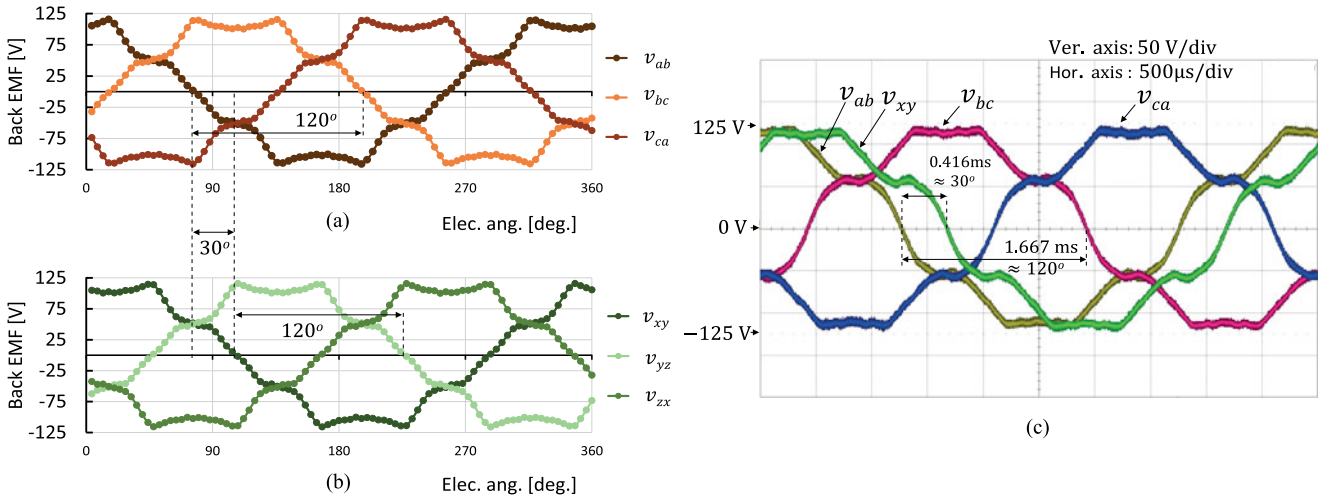

Fig. 10. Line-to-line back EMF of the six-phase IPMSM at 3000 r/min: (a) FEM result of abc phases, (b) FEM result of xyz phases, and (c) experimental results.

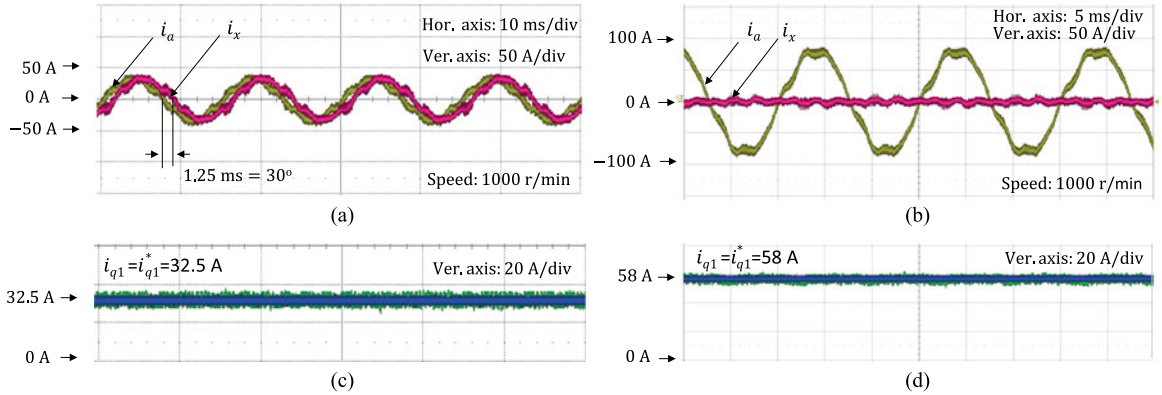

Fig. 11. Phase and dq currents when producing 20 N·m shaft torque at 1000 r/min: (a), (c) $(i^{e*}_{d1}, i^{e*}_{q1}) = (0, 32.5)$ A, $(i^{e*}_{d2}, i^{e*}_{q2}) = (0, 32.5)$ A, and (b), (d) $(i^{e*}_{d1}, i^{e*}_{q1}) = (-58, 58)$ A, $(i^{e*}_{d2}, i^{e*}_{q2}) = (0, 0)$ A.

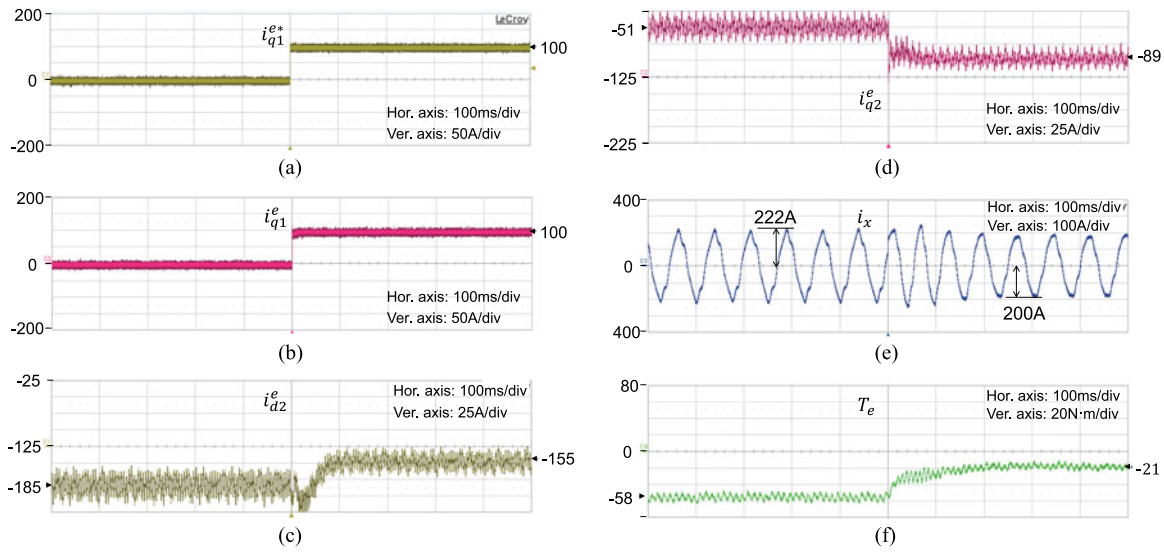

Fig. 12. Responses to a current step change when a three-phase inverter is connected to abc coils and xyz coils are shorted: (a) i^e_{d1}, (b) i^e_{q1}, (c) shaft torque T_e, (d) i^e_{d2}, (e) i^e_{q2}, and (f) x-phase current i_x.

TABLE VI
INDUCTANCE ESTIMATES

FEM analysis ($i_a = 250$ A)				Experiments (xyz coil shorted)			
L_{d1}	L_{q1}	L_{d2}	L_{q2}	L_{d1}	L_{q1}	L_{d2}	L_{q2}
106.3 μH	263.8 μH	145.8 μH	224.5 μH	107 μH	263 μH	146 μH	224 μH

TABLE VII
COMPARISON BETWEEN ANALYTIC RESULTS AND TORQUE MEASUREMENTS

Test conditions		Analytic				Exp.
Shorted	Regulated	T_{e1}	T_{e2}	T_{e12}	T_e	T_e
xyz	$(i^{*e}_{d1}, i^{*e}_{q1}) =$ (0, 0) A	0 N·m	-59.1 N·m	0 N·m	-59.1 N·m	-58 N·m
xyz	$(i^{*e}_{d1}, i^{*e}_{q1}) =$ (0, 100) A	30.6 N·m	-60.3 N·m	8.4 N·m	-21.3 N·m	-21 N·m

$(\mathbf{M}_f \mathbf{i}^e_{dq2})^*\}$, and $\frac{3P}{4}\text{Im}\{\mathbf{i}^e_{dq1} \cdot (\mathbf{M}_f \mathbf{i}^e_{dq2})^*\} + \frac{3P}{4}\text{Im}\{e^{j\frac{\pi}{6}} \mathbf{i}^e_{dq2} \cdot (e^{j\frac{\pi}{6}} \mathbf{M}^T_f \mathbf{i}^e_{dq1})^*\}$ terms from $T_{e1}, T_{e2},$ and T_{e12}, respectively. The reason is that the specified terms, which are a function of mutual components, establish themselves well in the system when both abc and xyz systems are functioning under the normal operating condition. It is obvious $T_{e1} = T_{e12} = 0$ and $T_{e2} = -59.1$ N·m for $L_{d2} = 146\,\mu$H, $L_{q2} = 224\,\mu$H, and $(i^e_{d2}, i^e_{q2}) = (-185, -51)$ A. T_{e2} is negative since braking torque was developed by the xyz coil. Note that the analytic data are quite close to the measured data (-58 N·m) of shaft torque. The same calculation procedure was applied to the case where $(i^e_{d1}, i^e_{q1}) = (0, 100)$ A. In this case, positive torque was developed by the abc coil, and $T_{e12} \neq 0$. Also in this case, the analytic torque is almost the same as the torque reading. Table VII shows a comparison between analytic calculations and the torque measurements.

VI. CONCLUSION

This work can be differentiated from the past study since it describe properly the dynamics of the six-phase IPMSM. The rotor saliency was taken into consideration by the abc and xyz coils differently reflecting the angle difference. The abc and xyz coils constitute two subsystems, but affecting each other. Two reference frames were involved to describe the dynamics of the six-phase IPMSM. Coupling between the two subsystems was handled by a coupling matrix $\mathbf{M}_f$. Also, a torque equation was derived completely using the two reference current variables. Three torque components were derived: one from solely by the abc coil, the second from solely by the xyz coil, and the third resulted from both.

Model verification was done in many steps throughout the paper. FEM flux results were compared with the flux model calculations. FEM torque and analytic torque were also compared. Finally, the model-based calculations were compared with the experimental data. Using the experimental data resulted from a shorted condition on xyz coils, all the necessary inductances were calculated, and they were used to predict the shaft torque. The computed torque was compared with the actual torque measurement, and it was observed that the two results agreed well remarkably. The vector control method suggested here provides a reference for the control of the IPMSM.

REFERENCES

[1] E. Levi, F. Barrero, and M. J. Duran, "Multiphase machines and drives-revisited," *IEEE Trans. Ind. Electron.*, vol. 63, no. 1, pp. 429–432, Jan. 2016.

[2] F. Demmelmayr, M. Troyer, and M. Schroedl, "Advantages of PM-machines compared to induction machines in terms of efficiency and sensorless control in traction applications," in *Proc. 37th Annu. Conf. IEEE Ind. Electron. Soc.*, Nov. 2011, pp. 2762–2768.

[3] J. Huang, M. Kang, J.-Q. Yang, H.-B. Jiang, and D. Liu, "Multiphase machine theory and its applications," in *Proc. 2008 Int. Conf. Electr. Mach. Syst.*, Oct. 2008, pp. 1–7.

[4] E. Levi, "Multiphase electric machines for variable-speed applications," *IEEE Trans. Ind. Electron.*, vol. 55, no. 5, pp. 1893–1909, May 2008.

[5] E. Levi, R. Bojoi, F. Profumo, H. A. Toliyat, and S. Williamson, "Multiphase induction motor drives—A technology status review," *IEEE Trans. Ind. Electron.*, vol. 1, no. 4, pp. 489–516, Dec. 2007.

[6] R. Bojoi, A. Tenconi, G. Griva, and F. Profumo, "Vector control of dual-three-phase induction-motor drives using two current sensors," *IEEE Trans. Ind. Appl.*, vol. 42, no. 5, pp. 1284–1292, Sep./Oct. 2006.

[7] Y. Zhao and T. A. Lipo, "Space vector PWM control of dual three-phase induction machine using vector space decomposition," *IEEE Trans. Ind. Appl.*, vol. 31, no. 5, pp. 1100–1109, Sep./Oct. 1995.

[8] K. B. Yadav, A. K. Mohanty, and P. Kumar, "Recent research trend on multi-phase induction machines," in *Proc. Int. Conf. Control, Commun. Power Eng.*, 2014, pp. 580–586.

[9] H. S. Che, E. Levi, M. Jones, W.-P. Hew, and N. Abd . Rahim, "Current control methods for an asymmetrical six-phase induction motor drive," *IEEE Trans. Power Electron.*, vol. 29, no. 1, pp. 407–417, Jan. 2014.

[10] P. Zheng, F. Wu, Y. Sui, P. Wang, Y. Lei, and H. Wang, "Harmonic analysis and fault-tolerant capability of a semi-12-phase permanent-magnet synchronous machine used for EVs," *Energies*, vol. 5, pp. 3586–3607, Sept. 2012.

[11] H. Kim, K. Shin, S. Englebretson, N. Frank, and W. Arshad, "Analytical model of multiphase permanent magnet synchronous machines for energy and transportation applications," in *Proc. 2013 Int. Electr. Mach. Drives Conf.*, Jan. 2013, pp. 172–179.

[12] A. S. Tomer and S. P. Dubey, "Performance analysis of two inverter fed six phase PMSM drive," in *Proc. 2013 Nirma Univ. Int. Conf. Eng.*, Nov. 2013, pp. 1–5.

[13] Y. Demir and M. Aydin, "A novel dual three-phase permanent magnet synchronous motor with asymmetric stator winding," *IEEE Trans. Magn.*, vol. 52, no. 7, Jul. 2016, Art. no. 8105005.

[14] F. Barrero and M. J. Duran, "Recent advances in the design, modeling, and control of multiphase machines-Part I," *IEEE Trans. Ind. Electron.*, vol. 63, no. 1, pp. 449–458, Jan. 2016.

[15] S. Kallio, M. Andriollo, A. Tortella, and J. Karttunen, "Decoupled d-q model of double-star interior permanent magnet synchronous machines," *IEEE Trans. Ind. Electron.*, vol. 60, no. 6, pp. 2486–2494, Jun. 2013.

[16] J. Karttunen, S. Kallio, P. Peltoniemi, P. Silventoinen, and O. Pyrhonen, "Decoupled vector control scheme for dual three-phase permanent magnet synchronous machines," *IEEE Trans. Ind. Electron.*, vol. 61, no. 5, pp. 2185–2196, May 2014.

[17] Y. Hu, Z.-Q. Zhu, and K. Liu, "Current control for dual three-phase permanent magnet synchronous motors accounting for current unbalance and harmonics," *IEEE J. Emerging Sel. Topics Power Electron.*, vol. 2, no. 2, pp. 272–284, Jun. 2014.

[18] Y. He, Y. Wang, J. Wu, Y. Y. Feng, and J. Liu, "A simple current sharing scheme for dual three-phase permanent-magnet synchronous motor drives," in *Proc. 2010 25th Annu. IEEE Appl. Power Electron. Conf. Expo.*, Feb. 2010, pp. 1093–1096.

[19] J. Su, J. Liu, and G. Yang, "Current control strategy for six-phase PMSM based on MPC under open-circuit fault condition," in *Proc. 2014 17th Int. Conf. Electr. Mach. Syst.*, Oct. 2014, pp. 1607–1611.

[20] Y. Lee and J.-I. Ha, "High efficiency dual inverter drives for a PMSM considering field weakening region," in *Proc. 7th Int. Power Electron. Motion Control Conf.*, Jun. 2012, pp. 1009–1014.
[21] E. Levi, "Advances in converter control and innovative exploitation of additional degree of freedom for multiphase machines," *IEEE Trans. Ind. Electron.*, vol. 63, no. 1, pp. 433–448, Jan. 2016.
[22] M. J. Duran and F. Barrero, "Recent advances in the design, modeling, and control of multiphase machines-Part II," *IEEE Trans. Ind. Electron.*, vol. 63, no. 1, pp. 459–468, Jan. 2016.
[23] T. Gerrits, J. L. Duarte, C. G. E. Wijnands, and E. A. Lomonova, "Twelve-phase open-winding SPMSM development for speed dependent reconfigurable traction drive," in *Proc. IEEE 10th Int. Conf. Ecological Veh. Renew. Energies*, Jun. 2015, pp. 1–7.
[24] T. Gerrits, C. G. E. Wijnands, J. J. H. Paulides, and L. Duarte, "Fault-tolerant operation of a fully electric gearbox equivalent," *IEEE Trans. Ind. Appl.*, vol. 48, no. 6, pp. 1855–1865, Nov./Dec. 2012.
[25] P. C. Krause, O. Wasynczuk, and S. D. Sudhoff, *Analysis of Electric Machinery*. Piscataway, NJ, USA: IEEE Press, 1995.
[26] K. H. Nam, *AC Motor Control and Electric Vehicle Applications*. Boca Raton, FL, USA: CRC Press, 2010.
[27] K. Zhang, H. M. Kojabadi, P. Z. Wang, and L. Chang, "Modeling of a converter-connected six-phase permanent magnet synchronous generator," in *Proc. 2005 Int. Conf. Power Electron. Drives Syst.*, Apr. 2005, pp. 1096–1100.
[28] J. Su, J. Yang, and G. Yang, "Mathematical model research of six-phase PMSM," *Adv. Mater. Res.*, vol. 614/615, pp. 1266–1271, Dec. 2012.

Muluneh Lemma Woldesemayat (S'16) was born in Fincha, Ethiopia, in 1981. He received the B.S. degree in electrical engineering from Arba Minch University, Arba Minch, Ethiopia, in 2004, and the M.Tech. degree in power electronics, electrical machines and drives from the Indian Institute of Technology Delhi, New Delhi, India, in 2009. He is currently working toward the Ph.D. degree in electrical engineering at Pohang University of Science and Technology, Pohang, South Korea.

His main research interests include analysis, modeling, and control of ac motor drive systems, specially related to permanent magnet synchronous motors in electric vehicle applications.

Heekwang Lee (S'14) was born in Seoul, South Korea, in 1988. He received the B.S. degree in electrical engineering from Chungnam National University, Daejeon, South Korea, in 2012. He is currently working toward the Ph.D. degree in electrical engineering at Pohang University of Science and Technology, Pohang, South Korea.

His research interests include the design, analysis, and control of power electronic systems, ac motor drives, and electric vehicles.

Sangchul Won (S'83–M'83) received the B.S. and M.S. degrees in electrical and electronics engineering from Seoul National University, Seoul, South Korea, in 1974 and 1976, respectively, and the Ph.D. degree in electrical engineering from the University of Iowa, Iowa City, IA, USA, in 1985.

He was a Visiting Assistant Professor with the University of Iowa, in 1985, and from 1985 to 1987, he was an Assistant Professor with the University of New Haven. He was a Visiting Professor with the Helsinki University of Technology, Espoo, Finland, in 2005, and with Osaka University, Suita, Japan, in 2009. He is currently a Professor with the Department of Electrical Engineering and Graduate Institute of Ferrous Technology, Pohang University of Science and Technology, Pohang, South Korea, where he is also the Director of the Steel Processing Automation Research Center. He has authored or co-authored more than 70 international SCI journal papers and 140 international conference papers. His research interests include time delay systems, control systems with uncertainties, robot control and steel-making process control, and automation.

Dr. Won served as the Chairman of the IFAC Mining, Mineral and Metal Processing Technical Committee in 2002–2008, and he is a Member of the IFAC Publication Committee. He also served as the President of the Institute of Control, Robotics and Systems, South Korea, in 2011. He was the President of the Asian Control Association in 2014–2015. He is an Associate Editor for the IEEE TRANSACTIONS ON INDUSTRIAL ELECTRONICS. He is the recipient of several awards, including a Korean Presidential Medal in 1994, the ICASE Academic Award, 2002, and the ICCAS Best Paper Award from the Minister of Knowledge and Economy.

Kwanghee Nam (S'83–M'86) received the B.S. degree in chemical technology and the M.S. degree in control and instrumentation engineering from Seoul National University, Seoul, South Korea, in 1980 and 1982, respectively, and the M.S. degree in mathematics and the Ph.D. degree in electrical engineering from the University of Texas, Austin, TX, USA, in 1986.

From 1998 to 2000, he was the Director of the Information Research Laboratories and the Dean of the Graduate School of Information Technology, Pohang University of Science and Technology, Pohang, South Korea, where he is currently a Professor with the Department of Electrical Engineering. Currently, he is the Director of the POSTECH E-Car Research Center, developing electric power trains. He is the author of a book, *AC Motor Control and Electrical Vehicle Applications* (CRC Press). His current research interests include ac motor control, power converters, motor design, and electric vehicles.

Dr. Nam was a recipient of the Best Transaction Paper Award from the IEEE Industrial Electronics Society in 2000 and the Second Best Paper Award at the 2014 IEEE Energy Conversion Congress and Exposition.